



## Effects of CO addition on the propagation characteristics of laminar CH<sub>4</sub> triple flame

Chih-Yung Wu<sup>a,\*</sup>, Yueh-Heng Li<sup>b</sup>, Tzu-Wei Chang<sup>c</sup>

<sup>a</sup> Department of Electro-Optical Science and Engineering, Advanced Engine Research Center, Kao Yuan University, Kaohsiung 82151, Taiwan, ROC

<sup>b</sup> Research Center for Energy Technology and Strategy, National Cheng Kung University, Tainan 701, Taiwan, ROC

<sup>c</sup> Department of Aeronautics and Astronautics Engineering, National Cheng Kung University, Tainan 701, Taiwan, ROC

### ARTICLE INFO

#### Article history:

Received 3 June 2011

Received in revised form 4 October 2011

Accepted 6 April 2012

Available online 11 May 2012

#### Keywords:

Blended fuel

Triple flame

Flame propagation

Numerical simulation

### ABSTRACT

This study proposes a numerical and experimental investigation of the propagation characteristics of CO-added CH<sub>4</sub> flames in a confined quartz tube. The transient propagation of a CH<sub>4</sub>/CO–air flames were modeled using GRI-Mech 3.0, and the propagation characteristics are discussed based on the calculated results. This study characterizes the formation of the reaction zone, the transformation of the flame base structure, the ignition of fuel, and the propagation phenomena of the leading point of the flame base. The leading point of methane flame with a large amount of added CO is found to be difficult to define unambiguously. During flame propagation, a complex combination of chemical reactions coupled with the fluid dynamics between the stoichiometric line and the preferred equivalence ratio line occurs. The results suggest that the leading point of the propagating flame is still dominated by the redirection effect, while the effect of the intrinsic chemical properties of the fuel mixture on a propagating flame has finite thickness cannot be neglected.

© 2012 The Combustion Institute. Published by Elsevier Inc. All rights reserved.

### 1. Introduction

In the attempt to replace with environmentally friendly, clean, and renewable energy sources, the use of gasified biomass, containing a mixture of carbon monoxide, hydrogen and methane, together with carbon dioxide and nitrogen, has become a versatile and attractive approach. It has become essential, therefore, to develop combustion techniques that can burn the gasified biomass or low-grade syngas effectively and to understand the chemical and physical properties of flames for this kind of fuel [1]. The particular composition of carbon monoxide in the gasified biomass is a major intermediate of hydrocarbon flames. Its combustion characteristics are different from those of alkanes, and can be characterized as “dry oxidation” and “wet oxidation” [2]. The intrinsic interaction between the original CO in the blended fuel and that produced from the oxidization of the hydrocarbons as well as the transition of chemical kinetics of the flame structure have been systematically investigated using an opposed-jet burner [1]. On the other hand, the study of flame propagation has been a topic of long-standing interest in combustion research. The interests and requirements arise both from the practical applications and from its important fundamental aspects. The flame stabilization mechanisms and propagation phenomena are important factors in developing rational burners, e.g., in diffusion flame combustors for power generation or in flaring stacks. A better understanding

of these phenomena is essential to improve models and to provide control strategies of combustion. This paper extends previous work on flame stabilization [3], and the flame structures of CH<sub>4</sub>/CO premixed fuels [1], studying the effect of CO addition on the propagation of laminar CH<sub>4</sub>–air triple flames to delineate its distinctive burning phenomena, as well as the propagation and flame structures.

Flame propagation, which is one of the significant factors controlling flame stability, is an issue of considerable fundamental importance to combustor design, and has been studied for several decades. Beginning in the 1960s, the triple flame has been observed [4] and studied for over five decades. It is believed that triple flames are responsible for flame propagation and stabilization in various nonpremixed or partially premixed stratified mixing layers. A schematic illustration of a triple flame is shown in Fig. 1a. As a fuel is stratified from a lean fuel to a rich fuel, a triple flame composed of a rich premixed flame branch and a lean premixed flame branch, together with a diffusion flame tail, propagates through the flow field. A tri-branchial point (triple point), which is the origin of the rich premixed flame branch, a lean premixed flame branch and a diffusion flame tail are assumed to propagate along a stoichiometric contour [5], which has been experimentally verified [6]. Consequently, several studies were proposed, which investigated the points of flow velocity [7], heat release [8], and fuel dilution [9,10]. There is significant experimental evidence demonstrating that the triple flame is the key stabilization mechanism not only for laminar but also for turbulent lifted flames [11]. In the past, few researchers paid much attention to the intrinsic properties of

\* Corresponding author. Fax: +886 6 6077906.

E-mail address: [cywu@cc.kyu.edu.tw](mailto:cywu@cc.kyu.edu.tw) (C.-Y. Wu).

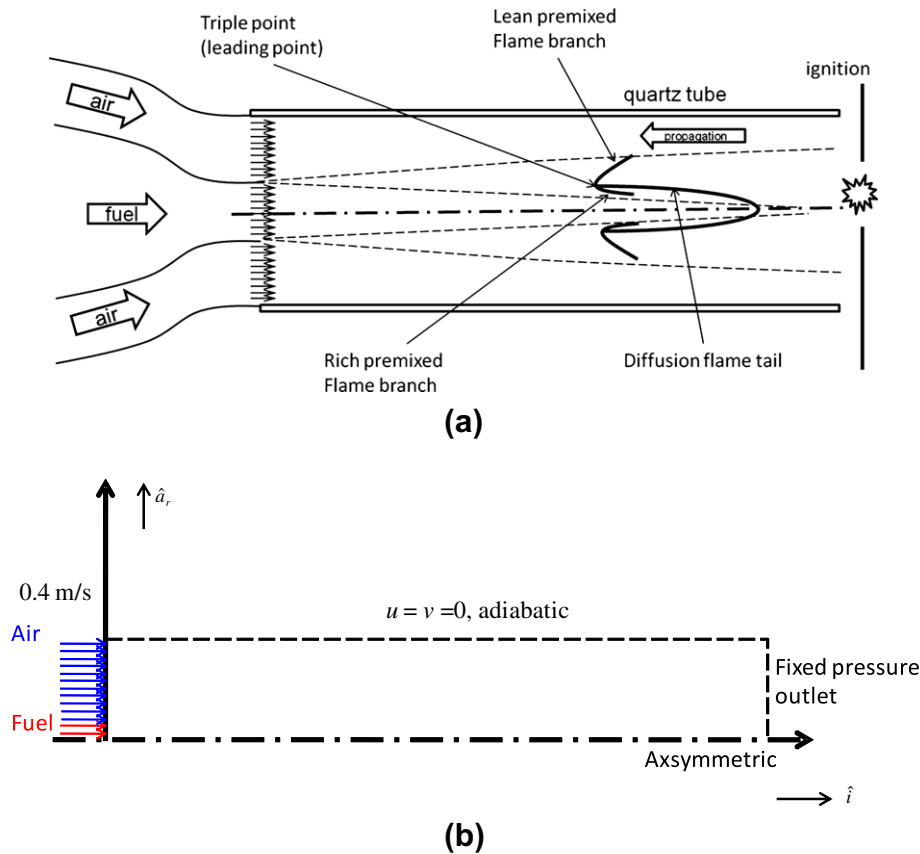


Fig. 1. Schematic illustration of (a) burner, triple flame structure and leading point, and (b) computation domain with boundary conditions.

the chemical reactions of fuel in triple flame investigations. For fuel containing additives, the effects of hydrogen enrichment on the propagation, flame structure, and dynamics of the triple flame structure also showed that the reaction rate of the flame is also concentrated near the triple point [8,13]. In triple flame propagation, the redirection effect [8] is the dominant factor and occurs at the triple point. Consequently, the flame tip and the leading point of a triple flame are also assumed to be situated at the same location. The results of a previous study [1] show that for a fixed fuel composition, the maximum burning velocity occurs at the rich side of the stoichiometry, and the maximum burning velocity increases with increasing CO concentration in the fuel mixture. In addition, the results also show that the effect of CO addition on the laminar burning velocity of the stoichiometric CH<sub>4</sub>/CO/air flames is mostly due to the transition of the dominant chemical kinetic steps and the heat release rate. Therefore, several questions arise in the flame propagation investigations for the fuel containing particular compositions: (1) Does the triple flame still propagate along a stoichiometric contour even though the laminar burning velocity of the rich premixed mixture is higher than that of the stoichiometric mixtures? (2) What is the interaction between the distributions of the mixture fraction and the propagation phenomena? (3) Is the triple flame structure deformed? (4) Most impor-

antly, does the triple flame still exist and is it dominant? By addressing these questions, a better understanding of the triple flame structure and propagation phenomena of carbon monoxide mixed with hydrocarbons can be gained, not only from a theoretical perspective but also for practical applications. This is the motivation of the present study to systematically investigate the effect of CO addition on the flame propagation of laminar CH<sub>4</sub>-air flames through both numerical simulations and experimental analysis. In the present study, the flame base traces of the triple flames for various amounts of added CO are first calculated and compared with experimental data to verify the exactness of the transient numerical simulations coupled with GRI-Mech 3.0 [14]. The computed heat release rate contours, mixture fraction contours, and flow field characteristics for different CO-added CH<sub>4</sub>-air propagating flames are presented. Furthermore, to clearly delineate the propagation path of the flame leading point, flame profiles along the stoichiometric mixture fraction and the preferred equivalence ratio lines are extensively compared in terms of significant species, reaction rate and heat release rate of the key reactions, as well as the total heat release rate. Finally, a mechanism is proposed to characterize and illustrate the formation of the reaction zone, the translation of the flame base structure, and the propagation phenomena of CO-added methane flame.

2. Methodology

## 2. Methodology

### 2.1. Burner and experiments

The experimental setup is shown schematically in Fig. 1a. The burner consists of central and coaxial jets, and the fuel and air

are modified by a well-contoured settling chamber. The diameters of the central and coaxial jets are 5 mm and 30 mm, respectively. A quartz tube 30 mm in diameter and 100 mm in length is attached to the exit of the burner. The fuel from the central jet operates at a fixed velocity of 0.4 m/s while the volumetric concentration of CO is varied from 0% to 96% in the blended fuel. The air velocity at the exit of the coaxial jet is also held constant at 0.4 m/s. Research-grade fuels are measured by electronic mass flowmeters and mixed in a mixing chamber prior to the settling chamber. The compressed air is filtered and dried using a refrigeration drier, and the dew point can be reduced to  $-20^{\circ}\text{C}$ . The uncertainties of the mass flowmeters for methane and carbon monoxide are  $\pm 1.0\%$  of the full scale. The conditions for the present investigations of the fuel–air triple flame propagation are listed in Table 1. The computed laminar burning velocities of the premixed  $\text{CH}_4/\text{CO}/\text{air}$  flames for different equivalence ratios under various  $\text{CH}_4/\text{CO}$  fuel compositions corresponding to the conditions which are listed in Table 1, are plotted [1] and shown in Fig. 2. For laminar flames, the flame base propagation velocity was predicted to be up to approximately  $3.5 S_L^{\circ}$  [13,14] while in turbulent flames the average value was reported to be in the range of  $1.8\text{--}3.5 S_L^{\circ}$  [15]. The maximum burning velocities of the fuel mixtures as well as the preferred equivalence ratio at which the maximum burning velocity occurs are listed in Table 1. To clarify the effect of the molecular diffusion of the stretched flame with different molecular weights, the Lewis numbers, which are defined as the ratio of thermal diffusivity to mass diffusivity for the mixture of methane, carbon monoxide and oxygen, are also shown in Table 1.

In the experiments, a high speed camera (PCO. 1200hs, Cooke Corp.) was used to capture the flame propagation process. To control the recording system precisely, both the camera and ignition device were triggered by a pulse/delay generator for synchronization. As the ignition device ignites the flame at the exit of quartz tube, the camera system is also triggered. The imaging frequency of the camera system is 500 Hz, and the images were stored in built-in RAM (4 GB). The images can be transferred to a PC for further analysis via the IEEE-1394 interface. The flame base is then identified with digital image processing, and the flame-propagation trace can be expressed as a function of time.

## 2.2. Numerical methods

To numerically model the transient propagation of the fuel–air flame, the time-dependent governing equations of continuity, momentum, energy, and chemical species are solved using the commercial package CFD-ACE+ coupled with chemical kinetic mechanisms from GRI-Mech 3.0 [16]. The molecular transport and thermal data are obtained from the CHEMKIN package [17]; the code then calculates the thermal conductivity and viscosity of the mixture using Wilke's formula. In addition, the gravitational effect is also included in the present study. The uniform flow of fuel and air at 0.4 m/s are specified at the inflow boundary of the computational domain. Fixed pressure boundary conditions are imposed on the open boundaries of the quartz tube exit. A non-slip, non-catalytic surface reaction and adiabatic conditions are applied to the quartz surface. The transport model also includes thermal diffusion to account for species diffusion due to temperature gradients. An axisymmetric, non-uniform staggered-grid system is used with a control volume formulation in accordance with the SIMPLE algorithm, which is shown schematically in Fig. 1b and c. To calculate the flame propagation coupled with GRI-Mech 3.0 effectively, a compromised grid was used in a grid-independence test. The total number of grids was 61 in the radial direction and 428 in the axial direction for a computational domain of  $15\text{ mm} \times 150\text{ mm}$  and a minimum grid spacing of 0.05 mm. The minimum grid size was placed near the axis and the fuel–air mixing layer, and an enlarged

grid size was used toward the outer boundaries. Convergence of the solution was declared when the ratio of the change of the dependent variables to the maximum variables in that iteration was less than  $1 \times 10^{-4}$ .

## 3. Results and discussion

### 3.1. Ignition, propagation phenomena and experimental validations

Figure 3 shows the ignition process of the numerical simulation. The steady state result of fuel–air mixing without a chemical reaction was solved in the first step and is shown in Fig. 3a. Figure 3b shows a hot zone as an ignition source for flame #1. To ignite the chemical reaction, the result shown in Fig. 3a was applied as the initial condition and a hot zone containing several significant intermediate species with a temperature of 1800 K was added to the computation domain near the outlet boundary. Following ignition, a reaction zone was formed, which propagates upstream. For pure methane flame propagation, the triple flame structure developed as the reaction zone propagated and approached  $x = 75\text{ mm}$ . The temperature contour and the fuel fraction contour are shown in Fig. 3c. To objectively validate the computed results using the experimental data, the origin is defined as the point at which the reaction zone reaches the axial location  $x = 70\text{ mm}$ . In experiments, the flame is ignited at the exit of the quartz tube. The flames propagate upstream, and their images are captured by high speed camera. Similar to the time trace of the numerical simulation, the origin is also defined in the same way. On the other hand, the velocity distribution in the flow field is very important for the present study. To clarify the flow field properties, the radial velocity distribution at  $x = 0, 25, \text{ and } 50\text{ mm}$  for flames #1 and #3 are shown in Fig. 4. The mixture flow is confined and develops in a tube. After the flow has been in the tube for a distance longer than the entry length, the fluid velocity varies with radial position, and the velocity at the wall approaches zero. Therefore, the flow in the center is actually faster for the same volumetric flow. In these cases, the density of the fuel jet is lower than that of the air coaxial flow. Due to buoyancy, flow acceleration near the centerline increases. As shown in Fig. 4, the velocities near the centerline at  $x = 50\text{ mm}$  for flames #1 and #3 are 0.513 m/s and 0.493 m/s, respectively. These two values differ by 3.8%.

The measured and computed temporal propagation traces, as well as the predicted propagation velocity of flame leading tip for four flames, are shown in Fig. 5. The results show that the propagation velocity increases as the amount of CO in the fuel stream is increased. However, the propagation velocity decreases at a 94% of concentration of CO in the fuel. It can be seen that the propagation velocity of the flame is in the range of 1.6 (flame #4)–3.46 (flame #3) times the maximum laminar burning velocity during the propagation process, with a near-constant velocity between  $x = 10\text{ mm}$  and  $x = 30\text{ mm}$ . In this region, the propagation phenomena are related to the laminar burning velocity and have the same tendency as the intrinsic maximum laminar burning velocity of the fuels shown in Fig. 2. The experimental verification shows that there is a good agreement between the measured and computed results for the case of flame #1. As expected, GRI-Mech 3.0 is optimized for methane and natural gas combustion. An over-prediction of the flame propagation traces is found for the cases of flames #2, #3, and #4, and the discrepancy increases as the amount of CO in fuel stream is increased. In practice, it is very difficult to obtain a mechanism that is suitable or optimized for the combustion of  $\text{CH}_4/\text{CO}$  fuels and or even for actual gasified biomass. Some papers that have studied syngas, gasified biomass, blended fuel and  $\text{C}_2\text{-alkane}$  experientially and applied GRI-Mech 3.0 to discuss flame phenomena and burning velocity [18–22]. Although GRI-Mech

**Table 1**  
Conditions of CO-added methane flame propagation in the investigation.

Flame case	Fuel		Maximum laminar burning velocity		Flammability limits (equivalence ratio)		Mixture fraction (labeled with no.)				Le <sub>O2</sub>	Le <sub>CH4</sub>	Le <sub>CO</sub>
	CH <sub>4</sub> (vol%)	CO (vol%)	m/s	Preferred $\phi$	Lean limit <sup>a</sup>	Rich limit <sup>b</sup>	1. $\phi$ = lean limit	2. $\phi$ = 1	3. $\phi$ = preferred $\phi$	4. $\phi$ = rich limit			
1	100	0	0.4024	1.1	0.5000	1.6700	0.0283	0.0551	0.0602	0.0887	1.08	0.89	N/A
2	70	30	0.4531	1.1	0.4520	3.2090	0.0409	0.0942	0.0451	0.2328	1.07	0.90	1.02
3	10	90	0.7654	1.7	0.4060	6.2870	0.1087	0.2310	0.3381	0.6540	1.07	0.94	1.04
4	4	96	0.7358	2.1	0.3464	6.5948	0.1104	0.2639	0.4296	0.7032	1.07	0.95	1.04

<sup>a</sup> Le Châtelier's rule.

<sup>b</sup> Prediction based on the composition of the fuel mixture.

3.0 has not been verified for other pure fuels or blended fuels, it is still an appropriate mechanism that serves the purpose of the present study. In addition, Fig. 5a also shows the results of grid-independence test. For five different grids, the simulations start using the same initial and boundary conditions. The difference between the results by  $428 \times 61$ ,  $500 \times 61$ , and  $550 \times 61$  are slight. Therefore, the  $428 \times 61$  was used for the present study.

The triple flame structure can be distinguished by the heat release rate [12,22]. Hence, the reaction zone in terms of heat release rate for the cases of flames #1, #2, #3 and #4 are used to identify the propagation and structural transformation of CO-added CH<sub>4</sub>-air flames, shown in Figs. 6, 7, 8, and 9, respectively. The four red<sup>1</sup> lines labeled with the numbers listed in Table 1 represent lean limit, stoichiometric, preferred equivalence ratio, and rich limit, and are also plotted in Figs. 6–9. Note that the first plot at  $t = 0$  ms corresponds to the instant at which the flame reaches  $x = 70$  mm. For the case of pure CH<sub>4</sub>-air (flame #1) flame propagation, the propagation is dominated by the triple point of the triple flame. The rich premixed flame branch, lean premixed flame branch and the diffusion flame tail can be clearly identified between  $x = 70$  mm and  $x = 40$  m. As the flame approaches even closer to the jet exit, the lean premixed flame branch appears to merge with the diffusion flame tail. On the other hand, the rich premixed flame branch forms a hollow cone flame structure during the propagation process from  $x = 70$  mm to 20 mm. When the flame is attached at the jet exit, the rich premixed flame can be distinguished, and the flame transforms from a triple flame structure to a diffusion attached jet flame. The computed process of the 100%CH<sub>4</sub>-air flame propagation is reasonably consistent with the theoretical prediction. The maximum heat release rate occurs at the triple point, and the triple point appears to propagate along the stoichiometric lines. It is interesting to note that the preferred equivalence ratio of CH<sub>4</sub> is 1.1, which is approaching its stoichiometric value. From the perspective of the global flame, the flame has a hollow cone structure during the propagation process in this case. For the case of pure 70%CH<sub>4</sub>/30%CO-air (case #2) flame propagation, in a similar manner to flame #1, the triple point of the triple flame still leads the flame propagation. The flame structure is clearly observed during the propagation process from  $x = 70$  mm to 40 mm. For the case of 10%CH<sub>4</sub>/90%CO-air flame (case #3), a different propagation phenomenon and flame structure is found. As the flame propagates further and approaches  $x = 66$  mm, the local laminar burning velocity decreases in the radial direction and has its maximum at the centerline; hence, the flame leading point moves to the central axisymmetric line. It is interesting to note that the flame appears to propagate along the stoichiometric line, even though the maximum burning velocity is still expected to occur along the centerline as it approaches  $x = 60$  mm. The reasons

for this distinctive phenomenon need to be clarified. As the flame propagates and reaches the preferred equivalence ratio mixtures, a hollow cone flame structure forms. The flame leading point and reaction zone, which has a higher heat release rate, congregate together and propagate along the preferred equivalence ratio line instead of along the stoichiometric line. In this case, the triple flame cannot be identified clearly, and the basic assumptions of the triple flame propagation phenomenon are inapplicable. Similar phenomena are also found for the case of 4%CH<sub>4</sub>/96%CO-air flame (case #4), as shown in Fig. 9.

Photographs of the 100%CH<sub>4</sub>- (flame #1), 70%CH<sub>4</sub>/30%CO- (flame #2), 10%CH<sub>4</sub>/90%CO- (flame #3), and 4%CH<sub>4</sub>/96%CO-air (flame #4) flame are shown in Fig. 10. The photographs correspond to the different flame cases from (a) to (d) and are shown when the flames are at  $x = 66$  mm. The flames at  $x = 50$  mm are shown from (e) to (h), and the flames at  $x = 30$  mm are shown from (i) to (l). According to these photographs, the apparent difference in the flame structures for the different fuel composition can be easily identified. For the cases of flames #1 (Fig. 10a, e, and i) and #2 (Fig. 10b, f, and j), the triple flame structure of the flame base is found. Unlike the structures of flames #1 and #2, in the case of flame #3 the flame appears to be a bullet-headed structure when it reaches  $x = 66$  mm. As the flame approaches  $x = 50$  mm, a hollow cone flame structure begins to form. As the flame approaches even closer to  $x = 30$  mm, a flame structure with a double flame layer is found. Finally, for the case of flame #4, the flame structures appear

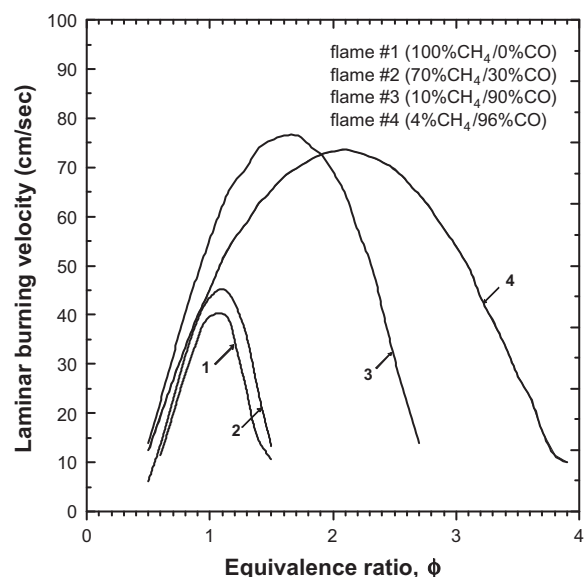


**Fig. 2.** Replot of laminar burning velocity versus equivalence ratio under different CH<sub>4</sub>/CO fuel compositions.

<sup>1</sup> For interpretation of color in Figs. 1, 3, 5–9, 11–15, the reader is referred to the web version of this article.

to be bullet-headed as the flame reaches  $x = 50$  mm and 60 mm. As the flame approaches  $x = 30$ , a hollow cone flame structure with a double flame layer similar to flame #3 is observed. It is interesting to note that the flame emission becomes brighter as the CO concentration is increased. The bright radiation from the flame for the cases with higher CO composition is induced by the decomposition of metal carbonyls [24]. Generally, the effect of decomposition of iron carbonyls is minor and has been discussed in a previous study [1]. Comparisons of the global flame structures in terms of the heat release rate with the captured flame images indicate that the numerical model can accurately predict the general flame characteristics. This certainly validates the proper settings of the boundary conditions in the model and also shows the capability of the combustion model and the mechanism used for the present CO-added CH<sub>4</sub>-air flame propagation calculations. This fact suggests that the model can be used for further analysis of chemical structures of the flame at the leading edge as the composition of fuel is varied.

### 3.2. Flame base structure and difficulty defining the leading point

To illustrate the triple flame structure of the propagating flame, the calculated H and heat release rate contours, the temperature and mixture fraction isopleths, and the velocity vectors are shown in Fig. 11 for flame cases #1 and #3 for when the flame reaches  $x = 30$  mm. The H contour, mixture fraction and temperature isopleths are shown on the upper side of the figure, while the lower side depicts the total heat release rate contour, mixture fraction isopleths, and velocity vectors. The mixture fraction isopleths labeled 1–4 represent the lean limit, stoichiometric, preferred equivalence ratio and rich limit, respectively. The purple isoline of the CO<sub>2</sub> mass fraction which accurately represents the overall shape of the triple flame and the maximum heat release isoline are also shown in Fig. 11. The isoline is used to calculate the displacement speed and is discussed in the following section. Note that the values of the CO<sub>2</sub> mass fraction are 0.073, 0.081, 0.110, and 0.152 for flame

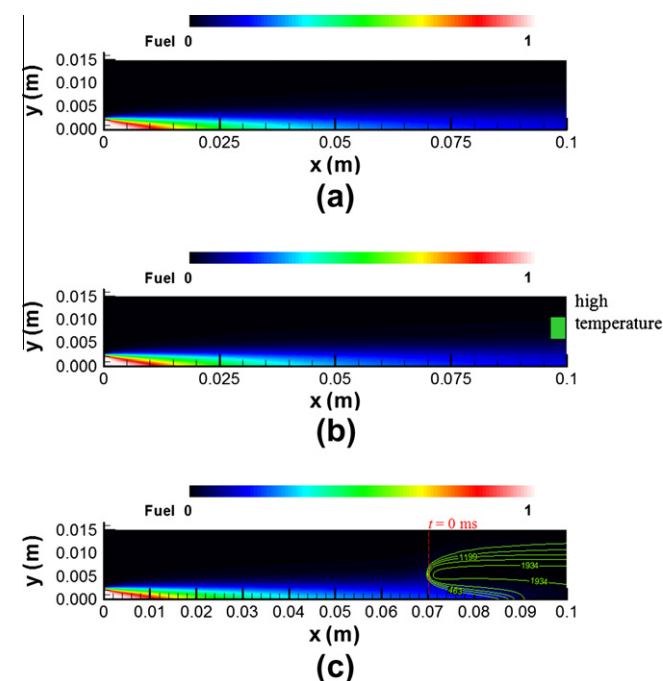


Fig. 3. Numerical simulation of ignition procedures: (a) contour of fuel-air mixing without reaction; (b) a high temperature zone was added to the ignition process; (c) contour of fuel-air mixing with temperature distribution corresponding to the flame reaching  $x = 70$  mm.

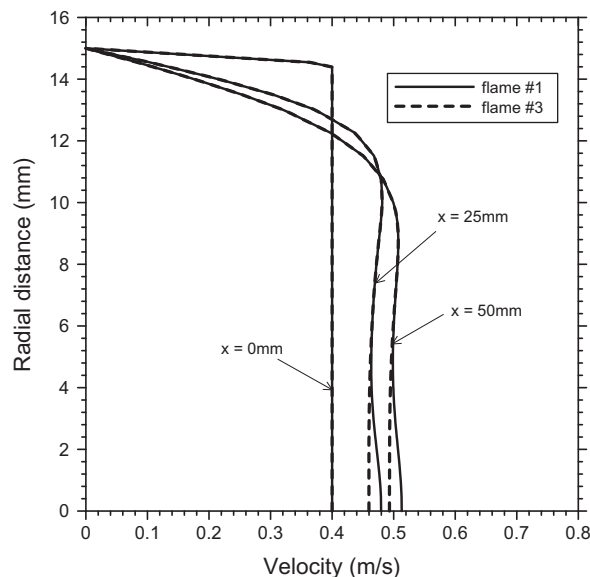


Fig. 4. Radial velocity distribution of cold flow at  $x = 0, 25,$  and  $50$  mm for flames #1 and #3.

cases #1, 2, 3, and 4 respectively. For the case of flame #1 shown in Fig. 11a, the triple flame structure can be identified based on the geometry of the contours of the heat release rate. Note that the contour levels are shown from 20 to 1530 MJ/m<sup>3</sup> s to clearly delineate the triple flame structure. By observing the peak region and the leading edge of the H atom and the isoline of the CO<sub>2</sub> mass fraction, it follows that the leading point of the triple flame propagates along stoichiometric isopleths. However, the distribution of the heat release rate contours shows that the peak region of reactivity is located near the preferred equivalence ratio ( $\phi = 1.1$ ) instead of along the stoichiometric isopleths. Correspondingly, the maximum burning velocity of pure methane peaks on the rich side near  $\phi = 1.1$  [25]. For the case of flame #3, which is shown in Fig. 11b, the flame structure based on the geometry of the contours of the heat release rate and the H atom is completely different to the case of flame #1. It is particularly interesting that the triple flame structure cannot be clearly identified in this case. For the heat release rate, the peak reactivity region is found to be located in the rich region and is wider than that of flame #1. It is necessary to note that the rich limit isopleths cannot be seen in the region shown in Fig. 11, and the mixtures in the rich region are combustible. In addition, a large number of H atoms are produced in the reaction zone in the rich region. According to the geometry of the heat release rate contours, the flame leading point is located on the preferred equivalence ratio isopleths but the isoline of the CO<sub>2</sub> mass fraction shows the leading point located between the stoichiometric and preferred equivalence ratio point.

To verify the ignition of fuel in front of the leading point, the flame base structure of the propagating flame for flames #1 and 3 in terms of the calculated H contours, the OH mixture fraction isopleths, and the mass flux of H and OH as well as the isoline of  $Y_{CO_2}$  are shown in Fig. 12. The mass flux of species  $i$  is defined as:

$$\bar{J}_i = -D_i \nabla Y_i = \frac{\partial}{\partial r} Y_i \hat{a}_r + \frac{\partial}{\partial x} Y_i \hat{i} \quad (1)$$

where  $D_i$  is the local diffusivity of species  $i$ . H and OH are produced in the flame reaction zone. Both play a significant role in inducing fuel destruction via upstream diffusion during flame propagation. In the case of flame #1 shown in Fig. 12a, both OH and H diffuse from the reaction zone in the upstream direction to initiate fuel dissociation reactions. It should be noted that, H and OH are

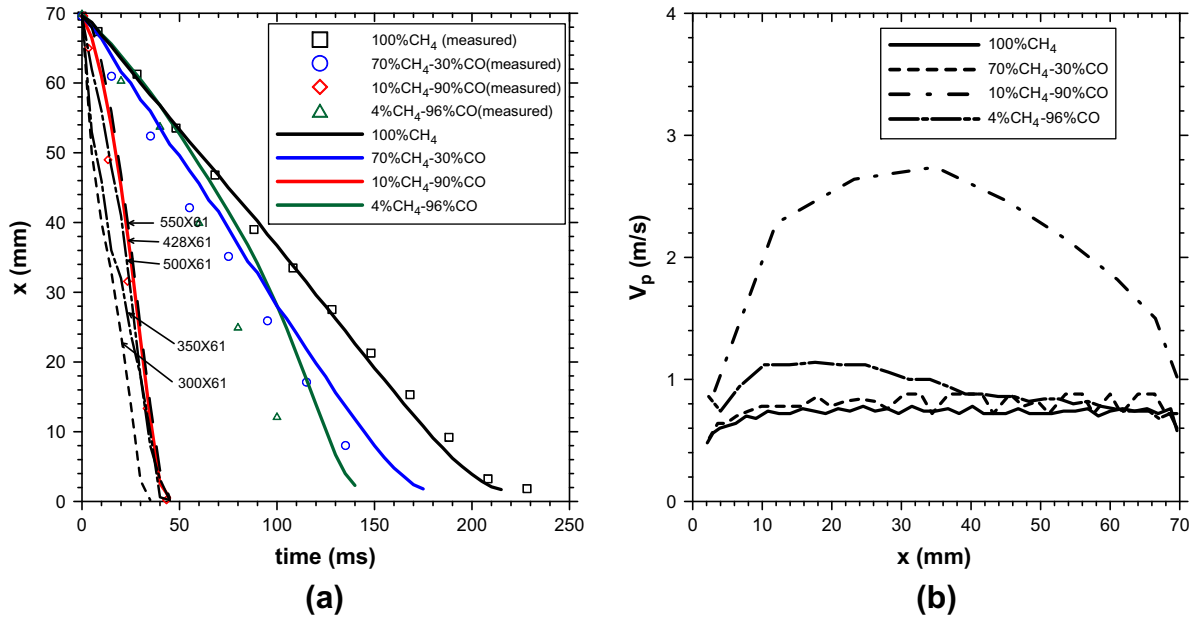


Fig. 5. (a) Measured and computed axial flame position; (b) predicted propagation velocity of flame leading tip as a function of distance from jet exit for four flames.

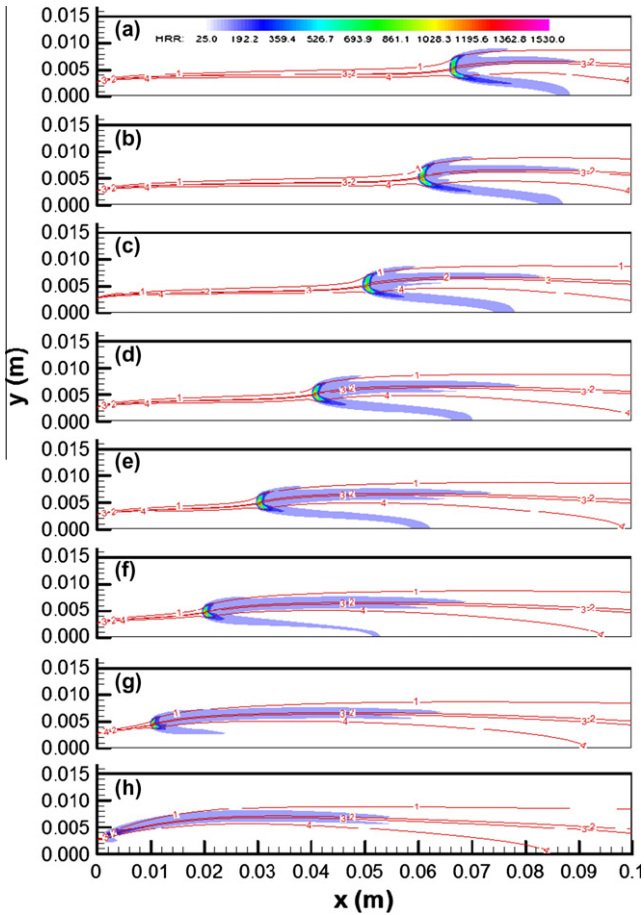


Fig. 6. Propagation and structural transformation of 100%CH<sub>4</sub> (flame #1)-air flames as the leading point approaches  $x =$  (a) 66; (b) 60; (c) 50; (d) 40; (e) 30; (f) 20; (g) 10; (h) 1 mm (rim).

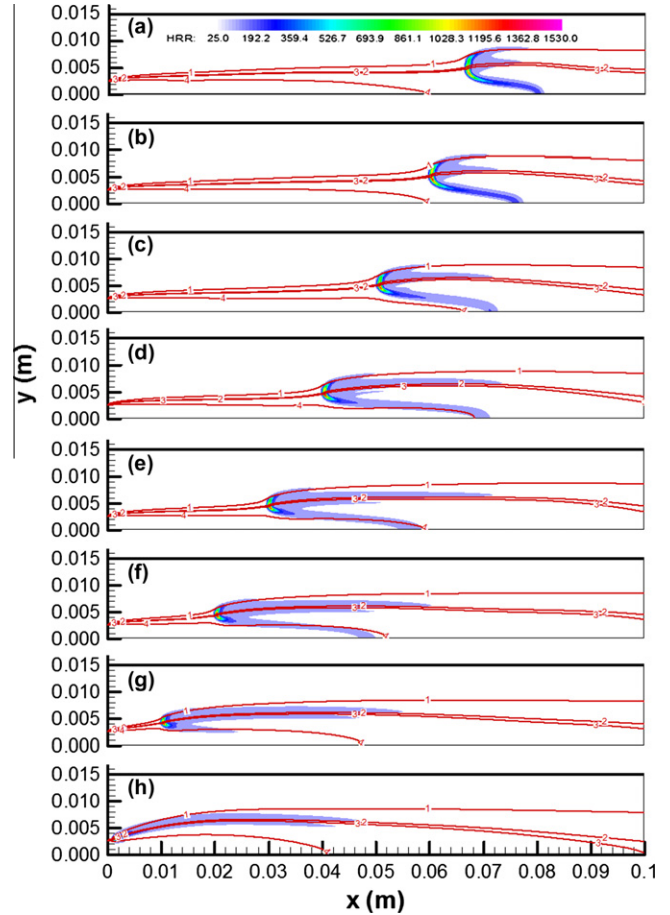
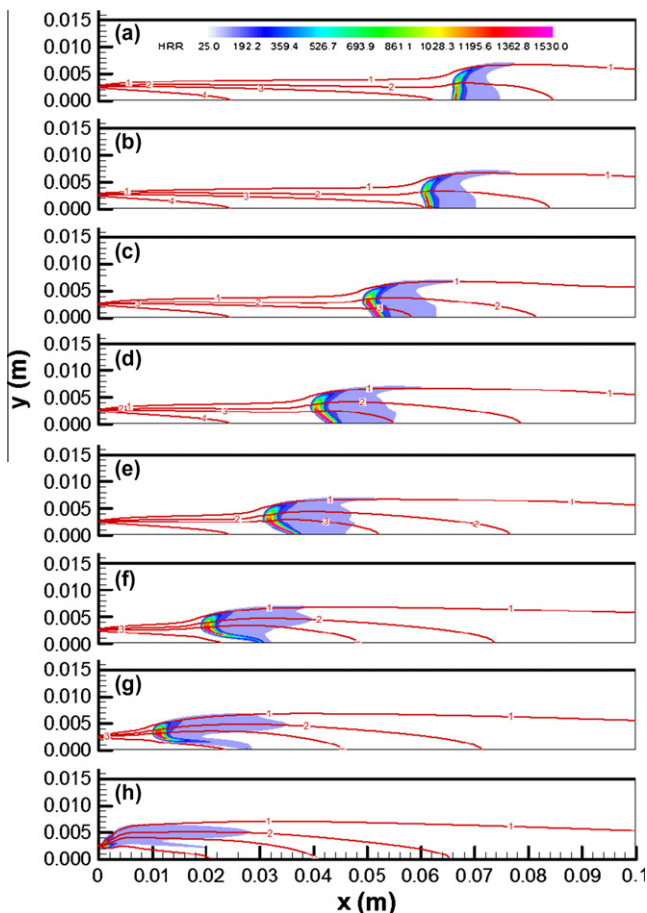


Fig. 7. Propagation and structural transformation of 70%CH<sub>4</sub>/30%CO (flame #2)-air flames as the leading point approaches  $x =$  (a) 66; (b) 60; (c) 50; (d) 40; (e) 30; (f) 20; (g) 10; (h) 1 mm (rim).

significant predominant species that induce and promote methane decomposition through R53 ( $H + CH_4 \leftrightarrow H_2 + CH_3$ ) and R98

( $OH + CH_4 \leftrightarrow CH_3 + H_2O$ ), and OH is the major species inducing the wet oxidation of CO through R99 ( $OH + CO \leftrightarrow H + CO_2$ ). OH and H



**Fig. 8.** Propagation and structural transformation of 10%CH<sub>4</sub>/90%CO (flame #3)-air flames as the leading point approaches  $x =$  (a) 66; (b) 60; (c) 50; (d) 40; (e) 30; (f) 20; (g) 10; (h) 1 mm (rim).

also diffuse in other direction to initiate other radical reactions. In the case of flame #3, which is shown in Fig. 12b, a large number of H atoms are yielded in the reaction zone of the rich region resulting in an abundance of H atoms diffusing in the upstream direction. The diffusion of H and OH upstream occurs in the rich-premixed zone, inducing a deformation of the triple flame structure and causing the leading point to move toward the preferred equivalence ratio line.

In order to delineate the ambiguous definition of the flame leading point and to simplify the comparison of the reaction of the flame profile along the preferred equivalence ratio line, the stoichiometric mixture fraction line, the mixture fraction line where the peak of CO<sub>2</sub> isoline is located, and the total heat release rate as the flames approach  $x = 30$  mm are shown in Fig. 13. For flame #3, the distribution of the total heat release rate along the preferred equivalence ratio line has a higher peak value and reaches  $x = 29.6$  mm; meanwhile, the distribution of the total heat release rate along the stoichiometric line and the line where the peak of CO<sub>2</sub> isoline is located only reaches  $x = 30.0$  mm and 30.4 mm respectively. For flame #1, the distribution of the total heat release rate along the preferred equivalence ratio line and the stoichiometric line reaches  $x = 30.0$  mm at the same time, but the former has a higher peak value. In addition, the distribution of the total heat release rate along the line where the peak of the CO<sub>2</sub> isoline is located is consistent with that along the stoichiometric line. The results show that the flame chemical reaction along the preferred equivalence ratio line is more active and generates more heat in both cases. However, most importantly, the results imply that

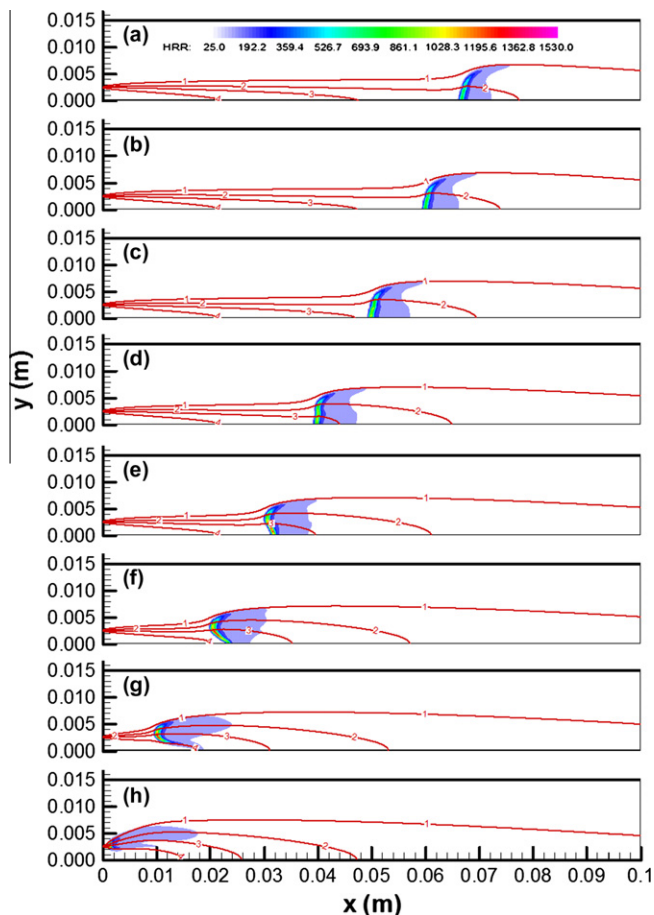


**Fig. 9.** Propagation and structural transformation of 4%CH<sub>4</sub>/96%CO (flame #3)-air flames as the leading point approaches  $x =$  (a) 66; (b) 60; (c) 50; (d) 40; (e) 30; (f) 20; (g) 10; (h) 1 mm (rim).

the definition of the leading point is ambiguous for flames in which a significant amount of CO has been introduced into the fuel mixture.

### 3.3. Flame dynamics

In order to examine the flow characteristics and flame dynamics, the local flame speed at the leading point which is defined based on the isoline of CO<sub>2</sub> mass fraction is extracted from the numerical simulation results [26]. In the present study, neither CH<sub>4</sub> nor CO properly represents the entire envelope of the triple flame front properly due to the composition of fuel mixtures; hence, the isoline of product concentration  $Y_{\text{CO}_2}$  is chosen, and the tip point of the  $Y_{\text{CO}_2}$  isoline is assumed to be a flame leading point. The density weighted flame speed determined from an isoline of species  $i$  is defined as:

$$S_d^* = \frac{\rho S_d}{\rho_u} = \frac{1}{\rho_u} \left( \frac{1}{|\nabla \phi|} [\nabla \cdot \Psi + \omega_\phi] \right) \quad (2a)$$

$$\Psi \equiv \rho D \nabla \phi \quad (2b)$$

where  $\rho_u$  denotes the density of the unburnt mixture, and  $D$  is the local mass diffusivity of species  $\phi$ . In the present study, the simulation domain is an axisymmetric system. The  $\nabla \phi$  and  $\nabla \cdot \Psi$  are individually defined as  $\frac{\partial}{\partial r} \phi \hat{a}_r + \frac{\partial}{\partial x} \phi \hat{i}$  and  $\frac{1}{r} \frac{\partial}{\partial r} (r \Psi) + \frac{\partial}{\partial x} \Psi$  for cylindrical coordinate system.  $S_d^*$  represents the local flame speed along the flame surface, while the local flame speed at the leading point yields the local triple flame speed ( $S_{tr}$ ) [9]. The normalized local triple

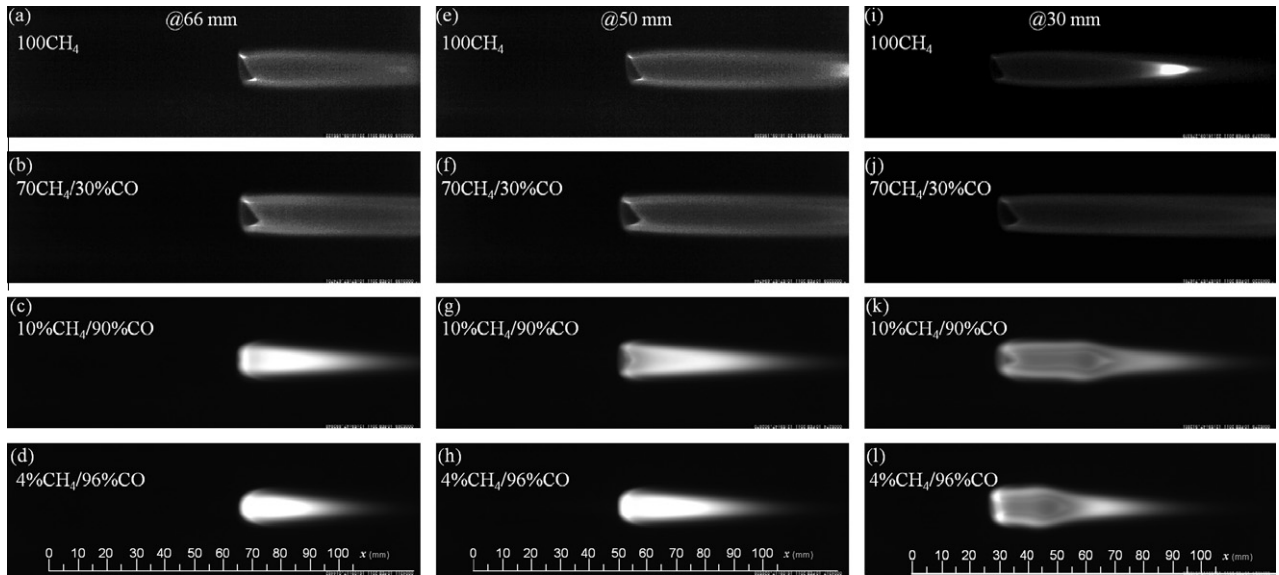


Fig. 10. Photographs of the 100%CH<sub>4</sub>- (flame #1), 70%CH<sub>4</sub>/30%CO- (flame #2), 10%CH<sub>4</sub>/90%CO- (flame #3), and 4%CH<sub>4</sub>/96%CO-air (flame #4) flames.

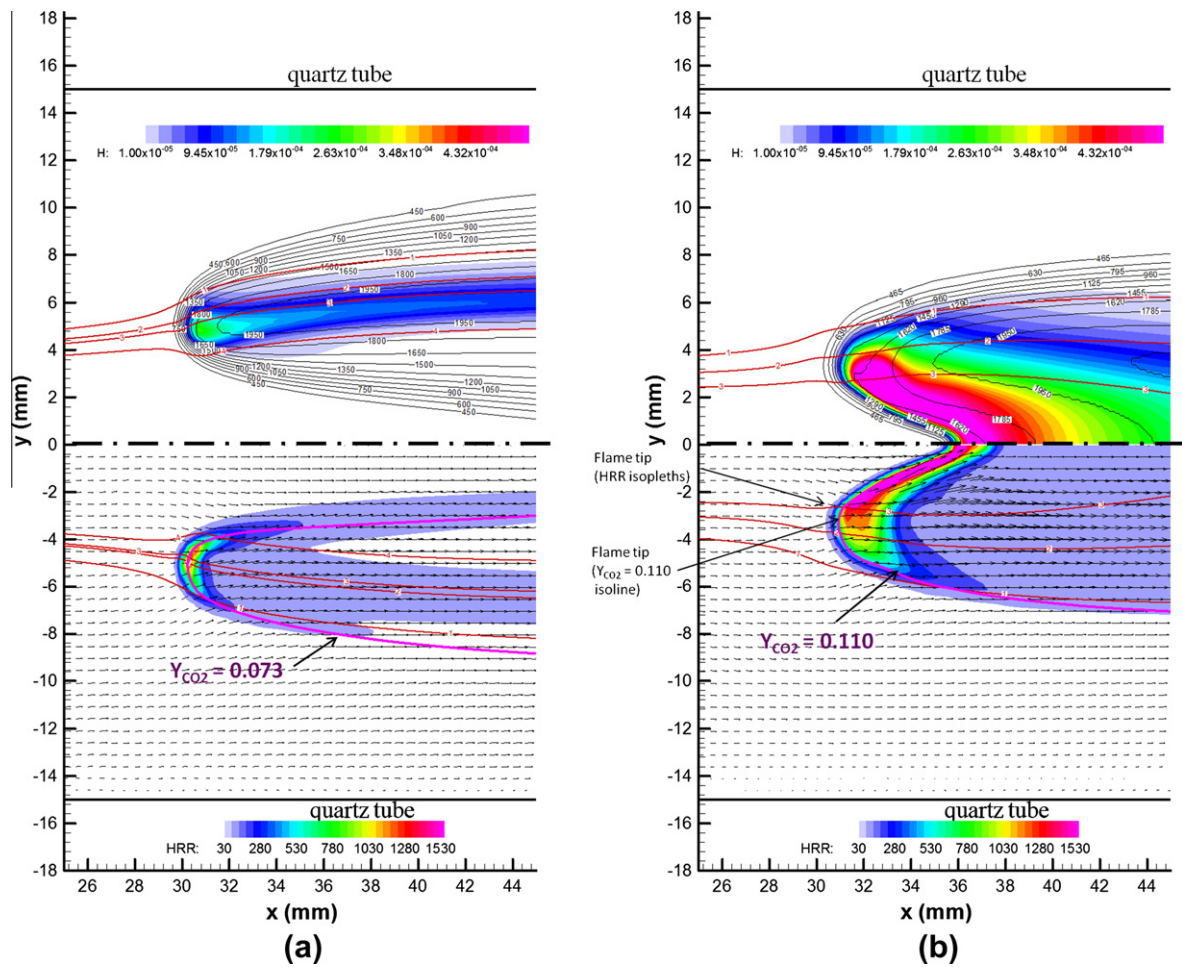


Fig. 11. Flame base structure of the propagating flame for flame #1 (a) and 3 (b) in terms of the calculated H and heat release rate contours, the temperature and mixture fraction isopleths, and the velocity vectors.

flame speed and the normalized global triple flame speed as a function of distance from the jet burner rim for the four flames are shown in Fig. 14a. Note that the local triple flame speed is normal-

ized by the stoichiometric laminar burning speed. As the amount of CO is increased, the normalized local triple flame speed increases due to the chemical reactivity. Chemical enhancement by adding

CO to the fuel mixture was proposed in our previous work [1]. The value of the normalized local triple flame speed is higher than unity for flames #3 and #4 during the propagation process, implying that the flame is affected by the chemical reaction and the shift of the maximum burning velocity. On the other hand, in order to verify the redirection effect and the square root of the density ratio, the normalized global flame speed as a function of distance from the burner rim for the four flames is shown in Fig. 14b. According to the simulation results, the square root of the density ratio for flames #1, #2, #3, and #4 is 2.708, 2.655, 2.421, and 2.398, respectively. The results show that  $U_F/S_{tri}$  is approximately equal to 2.4 for flames #1 and #2. This implies that the normalized global flame speed is proportional to the square root of the density ratio. For flames #3 and #4, the normalized global flame speed is approximately equal to 2.2 and 1.6, respectively, during flame propagation. Due to the limitations on the intrinsic properties of flame #3 and in particular #4, the length of the stoichiometric contour for flame #4 is much shorter as compared to #1 and #2. The flames in the case of flame #4 may still be in the developing stage, which may result in lower global propagation velocity.

The computed distributions of the velocity along the preferred equivalence ratio line and stoichiometric line for flame #3 are shown and labeled in Fig. 15. As the flame leading point approaches  $x = 66$  mm, the local laminar burning velocity decreases in the radial direction and has a maximum at the centerline. A “weak” redirection effect in the axial direction is found along the centerline. Since the flame is just ignited and has not been well developed, the redirection effect is not so apparent in axial direction. The density ratio between unburned and products is approximately equal to 2.4. Hence, the maximum point (center line) leads the flame (Fig. 8a) and the flow redirection effect near the stoichiometric line has not yet been found. As the flame approaches  $x = 60$  mm, the velocity distribution along preferred equivalence ratio line does not display the redirection effect as it does along the stoichiometric line. In this region, the flame just touches the preferred equivalence ratio mixtures, and the propagation of the flame leading point is still located at the stoichiometric line and is dominated by the flow redirection effect. The peak of the  $Y_{CO_2}$  isoline is also close to the stoichiometric line. As the flame propagates further to  $x = 30$  mm, the flame leading point begins to move toward the preferred equivalence ratio line due to chemical prop-

erties of the fuel. In this region, the propagation of the flame leading point is affected by the chemical reaction. It is interesting to note that, the flow redirection effect at the leading point is slightly stronger than that at stoichiometric line as the flame is well developed. The competition between the redirection effect and the chemical reactions is also shown in Fig. 8d. As the flame approaches  $x = 40$  mm for flame #4, double flame tips are found along the stoichiometric and preferred equivalence ratio line. Finally, as the flame propagates further upstream, the figures clearly show that the redirection effect still plays a central and dominant role in flame tip propagation. However, the flame leading point moves toward the preferred equivalence ratio mixture during propagation. For the propagation paths of the four flame cases and the flow field characteristics shown in Fig. 4, the flame base propagates within a near uniform flow field region. This implies that the effect of buoyancy is minor, and the influence of the velocity gradient generated in the flow field on the deformation of triple flame structure in the present study could be neglected.

### 3.4. Discussions

In the present study, numerical simulations coupled with detailed chemical mechanism as well as the transport and thermodynamic properties with experimental observations are performed to study a further realistic propagating flame and to examine the chemical affect on the flame propagation especially for triple flame characteristics. The flame is investigated under more complicated conditions compared to the research of Ruetsch et al. [8]; asymmetric jet flow confined in a quartz tube, flow development and buoyancy are also considered. For a typical triple flame, propagation is undoubtedly dominated by the flow redirection effect. The overall flame shape and heat release zone can be represented by an isoline of products, and the peak of the isoline is assumed to be the leading point, which propagates along the stoichiometric line. Furthermore, the region of peak reactivity is also assumed to be located at the triple point. For methane flame with a large amount of added CO, ambiguous definition of the leading point is observed. The flame propagates along the preferred equivalence ratio line if the leading point is defined based on the isopleths of heat release rate.  $CO_2$  is the oxidation product for both methane and carbon monoxide. If the leading point is defined based on

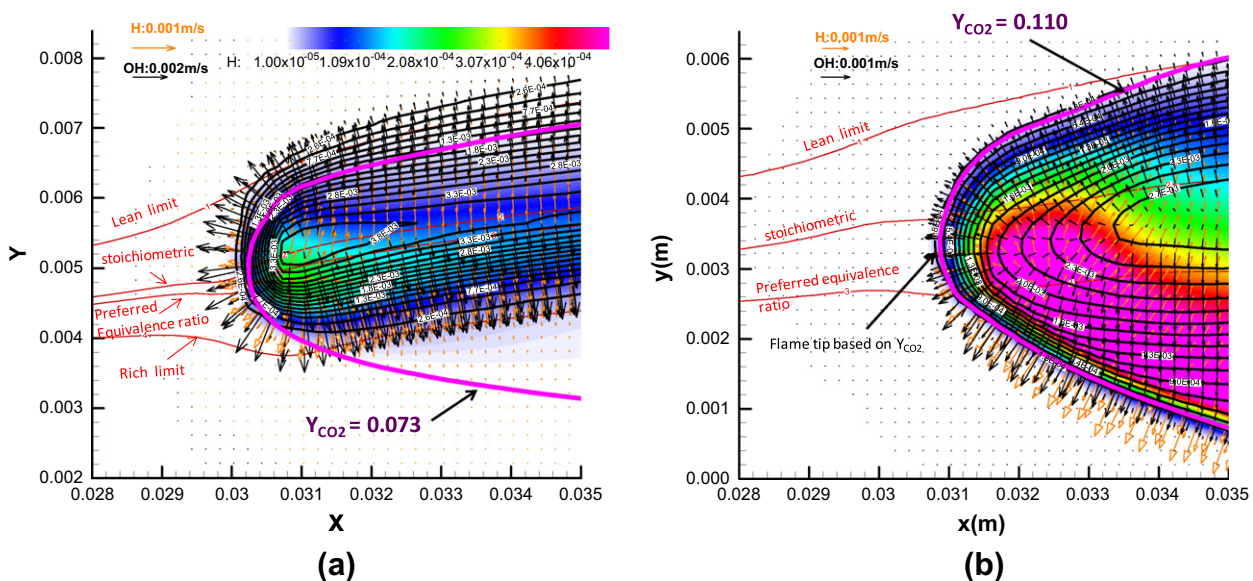
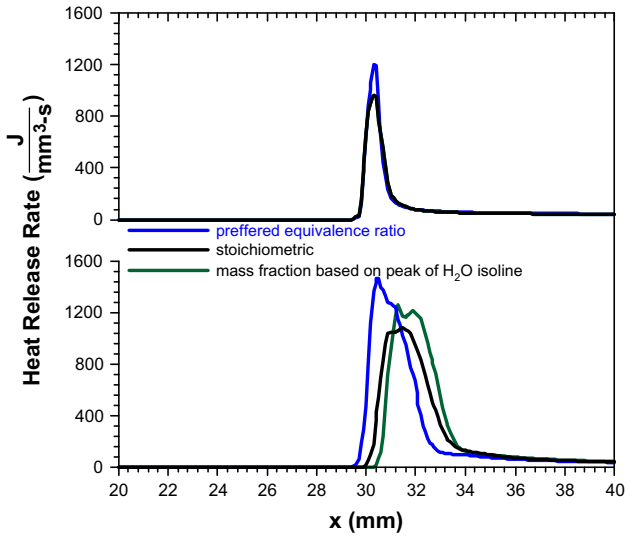


Fig. 12. Flame base structure of the propagating flame for flames #1 (a) and #3 (b) in terms of the calculated H contours, OH mixture fraction isopleths (black), and the flux of H (orange vectors) and OH (black vectors).



**Fig. 13.** Computed distributions of the total heat release rate along the preferred equivalence ratio, stoichiometric lines and the mass fraction line where the peak of the H<sub>2</sub>O isoline is located for: (a) flames #1 (100%CH<sub>4</sub>) and (b) #3 (10%CH<sub>4</sub>/90%CO).

the isoline of Y<sub>CO<sub>2</sub></sub>, the leading point is located between the stoichiometric line and the preferred equivalence ratio line. Although the definition of the leading point for a propagating flame has finite thickness that comprises various layers of different species at different locations is somewhat ambiguous and difficult, for a theoretical analysis of triple flame dynamics, we need to know which leading point dominates. Accordingly, the flame leading point is defined based on the tip point of the Y<sub>CO<sub>2</sub></sub> mass fraction isoline.

According to the present results, the redirection effect still plays an important role in flame propagation. Due to the enhanced chemical reaction in the rich premixed zone, the flame leading point is affected and moves toward the preferred equivalence ratio line. It is interesting that the redirection effect near the flame leading point is defined based on the isoline of Y<sub>CO<sub>2</sub></sub> is slight stronger than that near stoichiometric line as the flame is well developed. As noted, the fuel and air were completely consumed. It is believed

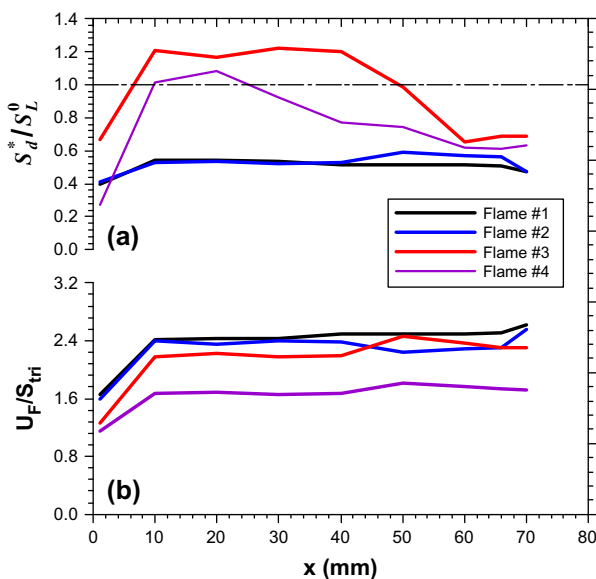


**Fig. 14.** Normalized local flame speed and (b) normalized global flame speed as a function of distance from jet exit.

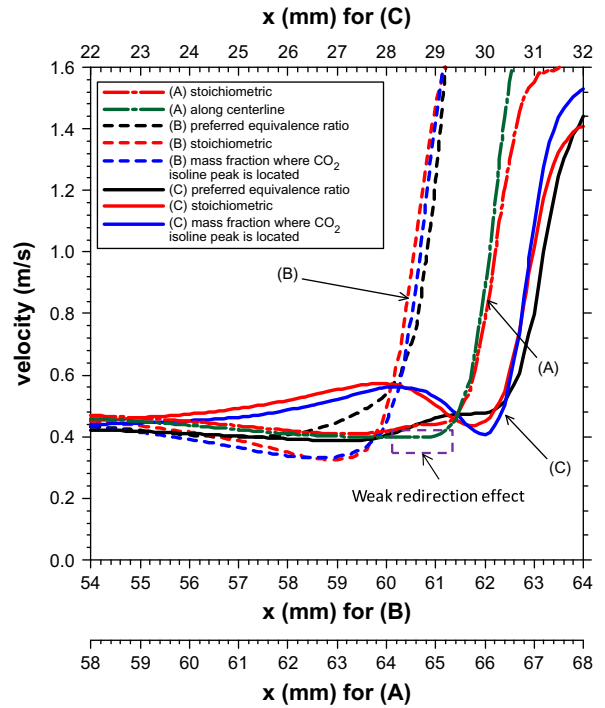


**Fig. 15.** Computed axial distributions of the axial velocity along the preferred equivalence ratio line (black) (solid), and the stoichiometric line (red), the mixture fraction line where the peak of CO<sub>2</sub> isoline is located (blue) (dashed), and the center line (green) for flame #3 as the leading point approaches x = (A) 66 mm (centered); (B) 60 mm (dashed); (C) 30 mm (solid).

that the competition of chemical reaction coupled with fluid dynamics between stoichiometric line and preferred equivalence ratio line occurs during flame propagation for methane flame with a large amount of added CO. Based on the current limited results, the leading point of a propagating flame is dominated both by the redirection effect and the intrinsic chemical properties of fuel mixture. This finding appears to raise doubts and questions concerning fundamental triple flame theories, which are worth addressing in future investigation. Even though the results suggest that the isoline of Y<sub>CO<sub>2</sub></sub> could represent the overall flame shape, and the peak can be regarded as the leading point of flame. The quantitative effect of the chemical reaction on propagation and movement of the flame front due to CO addition is still unclear.

**4. Conclusions**

In this study, a numerical investigation of the propagation characteristics of CO-added CH<sub>4</sub> flames in a confined quartz tube is presented. The transient propagation of a fuel–air flame is numerically investigated together with the complete chemical kinetic mechanisms of methane combustion. The predicted flame propagation traces are validated using instantaneous displacement measurement recorded by a high speed CCD camera. The effect of CO addition on the flame base structure and propagation phenomena are characterized:

1. After ignition, a reaction zone is formed, which propagates steadily upstream. The flame base traces show that the propagation velocity increases as the amount of CO in the fuel stream is increased. However, the propagation velocity decreases at a 94% concentration of CO in the fuel. The acceleration of the flame propagation for CO-added methane flame is dominated by the chemical reaction effect. Propagation phenomena are

- clearly related to the laminar burning velocity and have the same tendency as the intrinsic maximum laminar burning velocity of fuels. The validation also shows that the numerical simulation is appropriate for further detailed analysis.
- The flame base structure, the propagation traces and the profiles along the significant mixture fraction lines, the leading point of the flames which is defined based on the isoline of CO<sub>2</sub> mass fraction propagates along the mixture between the preferred equivalence ratio line and the stoichiometric mixture fraction line for methane flame with a large amount of added CO. However, the leading point of the flames, which is defined based on the isopleths of heat release rate, propagates along the preferred equivalence ratio line. The leading point of methane flame with a large amount of added CO is found to be difficult to define unambiguously. According the current results, the flame leading point can be defined based on the tip point of the Y<sub>CO2</sub> mass fraction isoline.
  - For methane flame with a low level of added CO, the global propagation of triple flame still obeys the square rule. For methane flame with a large amount of added CO, the propagation is not precisely proportional to the density ratio between reactants and products. Due to the limits of the intrinsic properties of methane flame with a large amount of added CO, the flame is still in the development stage because the length of stoichiometric contour is much shorter than in typical methane flame. This result appears to raise interesting questions concerning fundamental triple flame theories for such complex fuel, and these are worth addressing in future investigation.
  - The redirection effect always exists near the stoichiometric line, although the flame tip is located at a different location. It suggests that the redirection effect still plays an important role in flame propagation. Due to the enhanced chemical reaction in the rich premixed zone and the significant upstream diffusion of H and OH, the flame tip is affected and moves toward the preferred equivalence ratio line. In other words, during flame propagation of methane flame with a large amount of added CO, a complex combination of the chemical reaction coupled with fluid dynamics between the stoichiometric line and preferred equivalence ratio line occurs.
  - To be more specific, the evolutionary process of the propagation of CO-added methane flame is proposed. Based on the distribution of the isopleths of the mixture fractions as well as the effect of flow redirection and the chemical reactions, this paper char-

acterizes the formation of the reaction zone, the ignition of fuel, the transformation of the flame base structure, and the propagation phenomena of the jet flame base.

## Acknowledgments

This research was supported by the National Science Council of Republic of China under Grant Numbers NSC 99-2221-E-244-008-MY2 and NSC 99-2622-E-244-006-CC3. We are also grateful to the National Center for High-Performance Computing for computer resources and facilities.

## References

- C.-Y. Wu, Y.-C. Chao, T.S. Cheng, C.-P. Chen, C.-T. Ho, *Combust. Flame* 156 (2009) 362–373.
- J. Tröe, *Proc. Combust. Inst.* 27 (1998) 167–175.
- C.-Y. Wu, Y.-C. Chao, T.S. Cheng, Y.-H. Li, K.-Y. Lee, T. Yuan, *Combust. Flame* 145 (2006) 481–494.
- H. Philips, *Proc. Combust. Inst.* 10 (1965) 1277–1283.
- Y.S. Ko, S.H. Chung, *Combust. Flame* 118 (1999) 151–163.
- Y.S. Ko, S.H. Chung, G.S. Kim, S.W. Kim, *Combust. Flame* 123 (2000) 430–433.
- B.J. Lee, S.H. Jin, S.H. Chung, *Combust. Flame* 135 (2003) 449–462.
- G.R. Ruetsch, L. Vervisch, A. Liñán, *Phys. Fluids* 7 (1995) 1447–1454.
- A.J. Lock, A.M. Briones, X. Qin, S.K. Aggarwal, I.K. Puri, U. Hegde, *Combust. Flame* 143 (2005) 159–173.
- A.M. Briones, S.K. Aggarwal, V.R. Katta, *Phys. Fluids* 18 (2006) 043603.
- K.M. Lyons, *Prog. Energy Combust.* 33 (2007) 211–231.
- A.M. Briones, S.K. Aggarwal, V.R. Katta, *Combust. Flame* 153 (2008) 367–383.
- P.N. Kioni, B. Rogg, K.N.C. Bray, A. Liñán, *Combust. Flame* 95 (1993) 276–290.
- A. Liñán, E. Fernandez-Tarrazo, M. Vera, A.L. Sanchez, *Combust. Sci. Technol.* 177 (2005) 933–953.
- A. Upatnieks, J.F. Driscoll, S.L. Ceccio, *Proc. Combust. Inst.* 29 (2002) 1897–1903.
- G. Smith, D. Golden, M. Frenklach, N. Moriarty, B. Eiteneer, M. Goldenber, C. Bowman, R. Hanson, S. Song, W. Gardiner, V. Lissianski, Z. Qin, *GRI-Mech 3.0*, 1999. <[http://euler.me.berkeley.edu/gri\\_mech](http://euler.me.berkeley.edu/gri_mech)>.
- R.J. Kee, F. Rupley, J. Miller, et al., *User Manual, The CHEMKIN Collection Release 3.5*, Reaction Design, Inc., San Diego, CA, 1999.
- Fengsham Liu, Hongsheng Guo, Gregory J. Smallwood, *Combust. Flame* 133 (2003) 495–497.
- Fengshan Liu, Hongsheng Guo, Gregory J. Smallwood, Ömer Gü lder, *Combust. Flame* 125 (2001) 778–787.
- Vitali Lissianski, Vladimir Zamansky, George Rizeq, *Proc. Combust. Inst.* 29 (2002) 2251–2258.
- C.N. Vagelopoulos, F.N. Egolfopoulos, Paper WSS/CI 97S-022, Western States Section/Combustion Institute Meeting, Livermore, CA, April, 1997.
- I.C. McLean, D.B. Smith, S.B. Taylor, *Proc. Combust. Inst.* 25 (1994) 749–757.
- T.C. Williams, C.R. Shaddix, *Combust. Sci. Technol.* 179 (2007) 1225–1230.
- C.K. Law, *Combustion Physics*, Cambridge Univ. Press, New York, 2006.
- H.G. Im, J.H. Chen, *Combust. Flame* 119 (1999) 436–454.